

Prominence fine structures in a magnetic equilibrium

II. A grid of two-dimensional models

P. Heinzel^{1,2}, U. Anzer², and S. Gunár^{1,3}

¹ Astronomical Institute, Academy of Sciences of the Czech Republic, 25165 Ondřejov, Czech Republic
e-mail: [pheinzel;gunar]@asu.cas.cz

² Max-Planck-Institut für Astrophysik, Karl-Schwarzschild-Strasse 1, 85740 Garching, Germany
e-mail: ula@mpa-garching.mpg.de

³ Astronomical Institute, Faculty of Mathematics and Physics, Charles University, Prague, Czech Republic

Received 3 May 2005 / Accepted 1 July 2005

ABSTRACT

We construct a grid of 2D vertical-thread models for prominence fine structures which are in magnetohydrostatic (MHS) equilibrium. Such thread models have been described in a previous paper by Heinzel & Anzer (2001), but here we use a modified 2D transfer code with an adaptive MHS grid. Multilevel non-LTE transfer calculations are now performed for a 12-level plus continuum hydrogen model atom, in order to study the behaviour of the Lyman-series lines observed by SOHO/SUMER. Our grid consists of 18 models which cover a range of central column masses, magnetic-field intensities and two parameters characterising the 2D temperature structure of the thread. Since different Lyman lines and their parts (line center, peak, wings) are formed at different places within the thread, the Lyman series may serve as a good diagnostic tool for thermodynamic conditions varying from central cool parts to a prominence-corona transition region. We demonstrate this behaviour for various lines, showing their synthetic profiles as seen from two perpendicular directions along and across the magnetic field lines, respectively, and displaying the respective contribution functions. This study confirms our earlier conclusion that the Lyman line profiles are much more reversed when seen across the field lines, compared to those seen along the lines. The latter can be even unreversed. We also show the geometrical cross-section (shape) of all 18 models. Their thread-like shape with a considerable aspect ratio resembles recent high-resolution $H\alpha$ images. Finally, we discuss the relation of our thread models to the vertical threads studied by Fontenla et al. (1996, ApJ, 466, 496).

Key words. Sun: prominences – magnetohydrodynamics (MHD) – radiative transfer – line: profiles

1. Introduction

During almost one decade of observations SOHO (*Solar and Heliospheric Observatory*) has collected a large amount of UV and EUV data on prominences and filaments. Among them, spectral observations of hydrogen Lyman lines and continuum obtained by the SUMER UV-spectrograph represent an important constraint on prominence modelling. Various examples of such data and their analysis can be found in Schmieder et al. (1998, 1999, 2003) and Heinzel et al. (2001); see also a review of SOHO prominence observations by Patsourakos & Vial (2002). The formation depths of these optically-thick lines span the whole prominence structure and thus the line profiles of the Lyman series can provide us with a reliable diagnostics of prominence/filament thermodynamic conditions. The fact that SUMER is capable of observing the whole Lyman series is quite unique.

In order to interpret properly the Lyman-line profiles, one has to perform rather complex non-LTE radiative transfer computations using sophisticated models. Important steps towards

this goal were the following: magnetohydrostatic (MHS) and radiative-transfer models developed by Heasley & Mihalas (1976), first 2D prominence models by Mihalas et al. (1978) and Vial (1982), demonstration of importance of the partial frequency redistribution (PRD) for hydrogen Lyman lines (Heinzel et al. 1987), a grid of 1D models by Gouttebroze et al. (1993), 2D models with PRD (Paletou et al. 1993; Paletou 1995), multi-thread models in energy balance by Fontenla et al. (1996). Recently, Heinzel & Anzer (2001) (hereafter referred to as Paper I) have generalised the 1D MHS models of Heasley & Mihalas (1976) to the 2D case and have given examples of 2D diagnostics of vertical fine-structure threads in MHS equilibrium. Three important aspects play a role in the spectral-line formation: the pressure structure, the temperature variation in the *prominence-corona transition region* (PCTR) and the depth variations of the line source functions. The pressure structure is described by 2D MHS equilibria (for details see also Heinzel & Anzer 2005). The temperature profile is in principle determined by the energy balance, but here we model it by an ad hoc spatial variation and for the calculation of the source

function we perform the consistent 2D radiative transfer. Moreover, PRD plays an important role for the ionisation of hydrogen and affects the line intensities. The results of Paper I support the conclusions of Heinzel et al. (2001) that when looking *along* the magnetic-field lines the Lyman-line profiles appear as unreversed or only weakly reversed emission profiles, while when looking *across* the field lines, the profiles may exhibit rather strong reversals. This behaviour is due to the temperature structure of the PCTR.

However, so far no detailed quantitative fit of all observed Lyman lines (e.g. those presented for three different prominences in Heinzel et al. 2001) was achieved. It is the purpose of this paper to make further steps in our understanding of the behaviour of the Lyman spectrum formation. We construct here a grid of 18 fine-structure thread models, which are in 2D MHS equilibrium and have an infinite vertical extension. Selecting a set of input parameters allows us to demonstrate the sensitivity of individual models to various physical conditions. This experience will be used in the future to obtain a quantitative fitting of SOHO/SUMER Lyman spectra.

The paper is organised as follows. Section 2 summarizes the basic physical conditions inside the fine-structure thread and presents our 18 models. Section 3 describes the non-LTE radiative transfer in two dimensions, together with a new MHS adaptive-grid scheme. Section 4 explains how the so-called contribution functions can be used to visualize the line-formation regions. Section 5 gives a detailed discussion of our results obtained for individual models. Section 6 shows how the fine-structure dips can be seen in projection against the disk. Finally, Sect. 7 presents the discussion and the conclusions.

2. MHS models

For our modelling of prominence threads we use the form of vertically infinite 2D threads hanging in a horizontal magnetic field. The exact mathematical formulation of the equations of the MHS equilibrium was published in Paper I, here we give only an overview.

The pressure equation has the form

$$p(m, y) = 4p_c(y) \frac{m}{M(y)} \left[1 - \frac{m}{M(y)} \right] + p_0, \quad (1)$$

with the definition of the magnetic pressure

$$p_c(y) = \frac{B_{z1}^2(y)}{8\pi} \quad (2)$$

and with $M(y)$ (the column mass integrated over x -direction) given by

$$M(y) = \frac{B_x(y)B_{z1}(y)}{2\pi g}. \quad (3)$$

Here p_0 is the boundary coronal pressure, $B_x(y)$ is the horizontal field-component (constant along a given field line), $B_{z1}(y)$ is the vertical field-component at the boundary and g the gravitational acceleration at the solar surface. Because of the requirement of MHS equilibrium we have the relation

$$B_{z1}^2(y) = B_{x0}^2 - B_x^2(y). \quad (4)$$

Here B_{x0} is the horizontal field between individual threads. As in Paper I, we use the column-mass coordinate m instead of the cartesian coordinate x , which is more useful in the case of non-uniform temperature and ionisation structure. Then the transformation from the mass coordinate m to the spatial coordinate x requires the following integration

$$x = \int_{M(y)/2}^m \frac{1}{\rho} dm' \quad (5)$$

at each value of the coordinate y , where ρ is the density.

The temperature profile with an empirically described PCTR first used by Anzer & Heinzel (1999) has the form

$$T(m, y) = T_{\text{cen}}(y) + [T_{\text{tr}} - T_{\text{cen}}(y)] \left\{ 1 - 4 \frac{m}{M(y)} \left[1 - \frac{m}{M(y)} \right] \right\}^{\gamma_1}, \quad (6)$$

where T_{tr} represents the temperature at the boundary and the exponent γ_1 has to be chosen properly. The temperature at $x = 0$, $T_{\text{cen}}(y)$, is given by

$$T_{\text{cen}}(y) = T_{\text{tr}} - (T_{\text{tr}} - T_0) \left(1 - \left| \frac{y}{\delta} \right|^{\gamma_2} \right), \quad \text{for } |y| \leq \delta. \quad (7)$$

T_0 is the (minimum) central temperature, 2δ represents the width of the thread in y -direction (perpendicularly to the field lines) and the exponent γ_2 is again a free parameter. The 2D temperature structure is then fully determined by the exponents γ_1 and γ_2 .

The shape of synthetic spectral-line profiles obtained by radiative transfer modelling depends on the set of input parameters which describe the MHS equilibrium, the form of temperature structure, and on the incident radiation. The set of input MHS-parameters fully determines the shape of the magnetic dips and will influence the shape of the calculated synthetic profiles. The full description of all input MHS-parameters has been presented in Paper I. The first parameter which is varied in our calculations is the maximum column density M_0 appearing in the mass function $M(y)$

$$M(y) = M_0 \left(1 - \left| \frac{y}{\delta} \right|^{\gamma_3} \right), \quad \text{for } |y| \leq \delta. \quad (8)$$

Once we have prescribed M_0 we can use $B_x(0)$ (horizontal field in the middle of the thread) instead of B_{x0} (horizontal field between threads), where the former one represents a measurable quantity for prominences. The values of B_{x0} and $B_x(0)$ are simply related through Eqs. (3) and (4).

In order to describe the dependence of the synthetic profiles on given input parameters we have constructed a grid of 18 prominence models. Within this grid of models we varied M_0 , $B_x(0)$ and the exponents γ_1 and γ_2 . The other input parameters have been fixed for all our models, with the values:

$$T_0 = 8000 \text{ K}; \quad T_{\text{tr}} = 50000 \text{ K}; \quad 2\delta = 1000 \text{ km}; \\ \gamma_3 = 2; \quad p_0 = 0.03 \text{ dyn cm}^{-2}.$$

The model grid consists of three series with 6 models for each of them. The series differ only in the value of one of the γ -parameters. The models in each series have different values of M_0 and $B_x(0)$. The full list of our model grid

Table 1. Parameters for the model grid.

Models of series A	Models of series B	Models of series C	M_0 [g cm ⁻²]	$B_x(0)$ [Gauss]
$\gamma_1 = 5$	$\gamma_1 = 10$	$\gamma_1 = 10$		
$\gamma_2 = 30$	$\gamma_2 = 60$	$\gamma_2 = 30$		
A ₁	B ₁	C ₁	2×10^{-4}	8.4
A ₂	B ₂	C ₂	5×10^{-5}	4
A ₃	B ₃	C ₃	2×10^{-5}	2
A _{3_1}	B _{3_1}	C _{3_1}	2×10^{-5}	10
A ₄	B ₄	C ₄	5×10^{-6}	1
A _{4_1}	B _{4_1}	C _{4_1}	5×10^{-6}	5

is summarised in Table 1. Geometrically all these models represent structures with a width of 1000 km and their lengths vary between 2000 km and 25 000 km which partially depends on the solution of the radiative-transfer problem (see below). An example of the 2D variation (in the $x - y$ plane) of the temperature, gas pressure and density and of the magnetic structure is shown in Paper I.

3. 2D multilevel radiative transfer

For the solution of the 2D radiative transfer problem we used the Accelerated Lambda Iteration (ALI) technique (Auer & Paletou 1994) with the short characteristics (SC) method to obtain the formal solution along individual rays. A detailed description of the method is given in Paper I.

In contrast to our previous paper we use here a 12-level plus continuum hydrogen model atom (see e.g. Heinzel et al. 1997), in order to obtain higher members of the Lyman series as they are observed by SOHO/SUMER. The 12-level model also ensures a higher accuracy as compared to the 5-level model (at least of lower Lyman lines) because of more precisely computed level populations.

In Figs. 1 and 2 we show averaged profiles of the $L\beta$ and $L\delta$ lines, in order to compare the 5-level and 12-level solutions. Full lines result from averaging along the dip thickness 2δ , dashed lines represent averaging along the whole dip length (i.e. in the x -direction). The difference in intensities is given by the different level populations, while the ionisation is almost the same for the two cases.

3.1. Incident radiation at the thread boundary

Lyman-line profiles of the incident radiation are taken from the SOHO/SUMER disk observations made by Warren et al. (1998). The observed profiles show an asymmetry due to flows in the solar atmosphere, however, for our purposes we used quiet-Sun profiles symmetrised by averaging the red and blue parts. Since Warren et al. (1998) data do not include the $L\alpha$ line (this line was difficult to detect with SUMER), we still use the same incident profiles as in the previous Paper I. The averaged incident radiation was computed at height of 10 000 km above the solar surface.

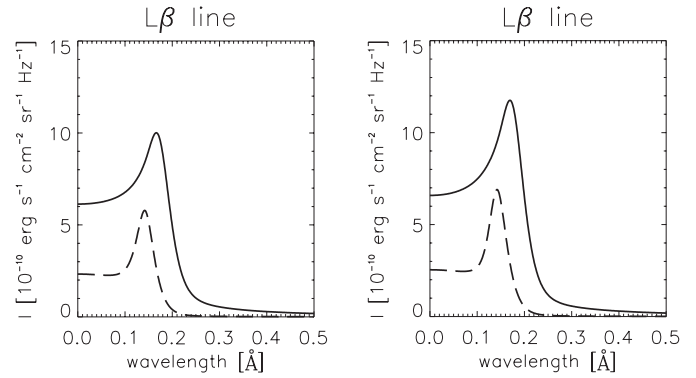


Fig. 1. $L\beta$ profiles for the 5-level model (left-hand side) and for the 12-level model (right-hand side). Full lines represent averages over y , dashed lines are mean profiles over x .

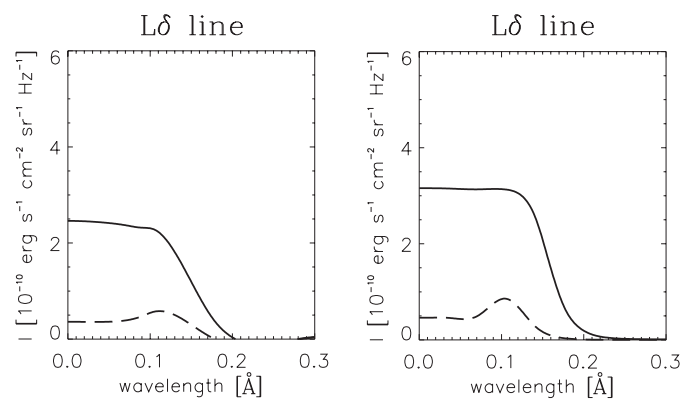


Fig. 2. $L\delta$ profiles for the 5-level model (left-hand side) and for the 12-level model (right-hand side). Full lines represent averages over y , dashed lines are mean profiles over x .

3.2. Adaptive MHS grid

A new feature of the present models is that we use here an *adaptive* MHS grid. In the y -direction the grid is fixed and we use the logarithmic spacing in order to properly describe a steep PCTR at the boundary. However, in the x -direction, i.e. along the field lines, the geometrical extension of the magnetic dip follows from the MHS equilibrium – for a given field strength, the larger M_0 the deeper the dip will be (and thus the structures are effectively less extended). Moreover, the conversion from the column-mass coordinate m as used to express the MHS equilibrium (Paper I) to geometrical one needed for 2D radiative transfer, depends on the local gas density which in turn depends on the ionisation degree. In Paper I we just used an initial estimate of the ionisation degree (see Eq. (17) in Paper I) and kept the x -grid fixed. In this paper we follow the procedure described in Heinzel & Anzer (2003). After the converged non-LTE solution is obtained for a given 2D model, and thus 2D distribution of the ionisation degree, a new grid is constructed along the field lines which is consistent with the current ionisation degree. Then the 2D transfer is solved again to get a new ionisation degree and this procedure is repeated until the changes between two subsequent grids are negligible. Typically 5 iterations are sufficient. For more details see Heinzel & Anzer (2003).

4. Contribution function

For the analysis of the diagnostic properties of the Lyman lines we need to know the corresponding formation depths. For this purpose we use the contribution function C . This function for the emergent specific intensity is defined by the integral relation

$$I_{\nu}(0) = \int C_1(l)dl, \quad (9)$$

where l is the geometrical length (depth) which we take here either in x or y -direction. In terms of the optical depth τ_{ν} the contribution function is defined as

$$C_1(\tau_{\nu}) = S_{\nu}(\tau_{\nu})e^{-\tau_{\nu}}. \quad (10)$$

The transformation between optical depth τ_{ν} and geometrical depth l is given by

$$C_1(l)dl = C_1(\tau_{\nu})d\tau_{\nu}. \quad (11)$$

Then the contribution function has the form

$$C_1(l) = S_{\nu}(\tau_{\nu})e^{-\tau_{\nu}}\chi_{\nu}. \quad (12)$$

Here χ_{ν} represents the absorption coefficient. Since the source function is given by $S_{\nu} = \eta_{\nu}/\chi_{\nu}$, we obtain

$$C_1(l) = \eta_{\nu} e^{-\tau_{\nu}}, \quad (13)$$

with η_{ν} being the emission coefficient.

The contribution to the specific intensity on the surface from a given point of the geometrical grid depends on the direction of the line-of-sight. In this paper we display the contributions as functions of x and y for two perpendicular directions of view: along x -coordinate (along the field lines) and along y -coordinate (across the field lines). 2D plots of computed contribution functions, for all considered Lyman lines, are available on the web site <http://www.asu.cas.cz/~radtrans>. Examples are shown below for selected models, lines and positions in the line profile (line center, peaks, wings). These plots show the spatial variation of the contribution to the specific intensity as a function of the position in the structure of the prominence ($x - y$ dimensions are in cm). White regions represent places with major contribution to the specific intensity (for a given frequency), black regions indicate minor contributions. The contours in the figures are iso-lines of the temperature structure. Isothermal contours are plotted in steps of 10 000 K. Note that these figures are not drawn to the true scale.

5. Synthetic profiles

In this section we discuss the dependence of our synthetic profiles on the values of the input parameters defining individual models, as well as their variation with the viewing direction. All line-profile plots are also available at <http://www.asu.cas.cz/~radtrans>.

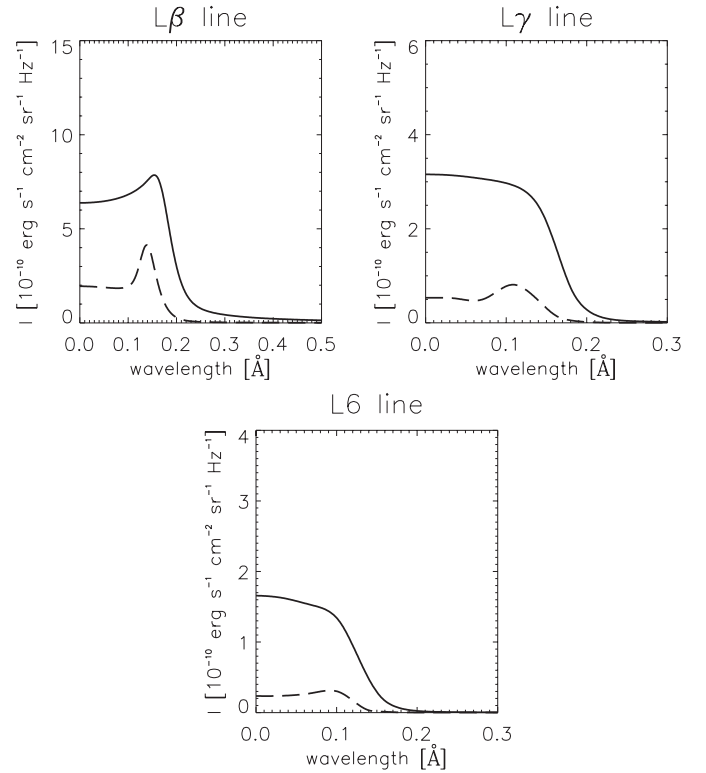


Fig. 3. The profiles of lines $L\beta$, $L\gamma$ and $L6$. Full lines are y -mean profiles, dashed lines are x -mean profiles.

5.1. Dependence on the field orientation

As was shown in Heinzel et al. (2001), the computed Lyman-line profiles of prominences strongly depend on the viewing angle with respect to the magnetic-field orientation. Paper I contains one example of a synthetic profile computed for a specific model with a 5-level atom. Here we show synthetic profiles obtained for our grid of models using an extended 12-level hydrogen atom.

In Fig. 3 we show $L\beta$, $L\gamma$ and $L6$ line profiles. Full lines again represent profiles averaged over y , dashed lines are profiles averaged over x . The intensity plots (Fig. 4) show the variation of the line intensity as a function of x and wavelength. Each profile there represents a mean profile averaged locally over 1000 km in x -direction.

The field orientation has a two-fold effect on the Lyman-line shapes. First, the density distribution *along* the field lines is given by the MHS equations, while *across* the field lines the column mass $M(y)$ can vary in a rather arbitrary way because the individual flux tubes are magnetically separated. For the variation of $M(y)$ we use an ad hoc form described by Eq. (8). Second, along the field lines the temperature variation is supposed to be relatively smooth because of efficient heat conduction – we describe this variation by an empirical formula (6). On the other hand, the heat conduction across the field lines is strongly inhibited and thus we assume a schematic temperature profile (7) which exhibits a rather steep rise at the boundaries.

From our grid of models we conclude that the $L\alpha$ profiles are rather similar when one looks along the x -axis and when one looks in y -direction. But for all higher lines we see that

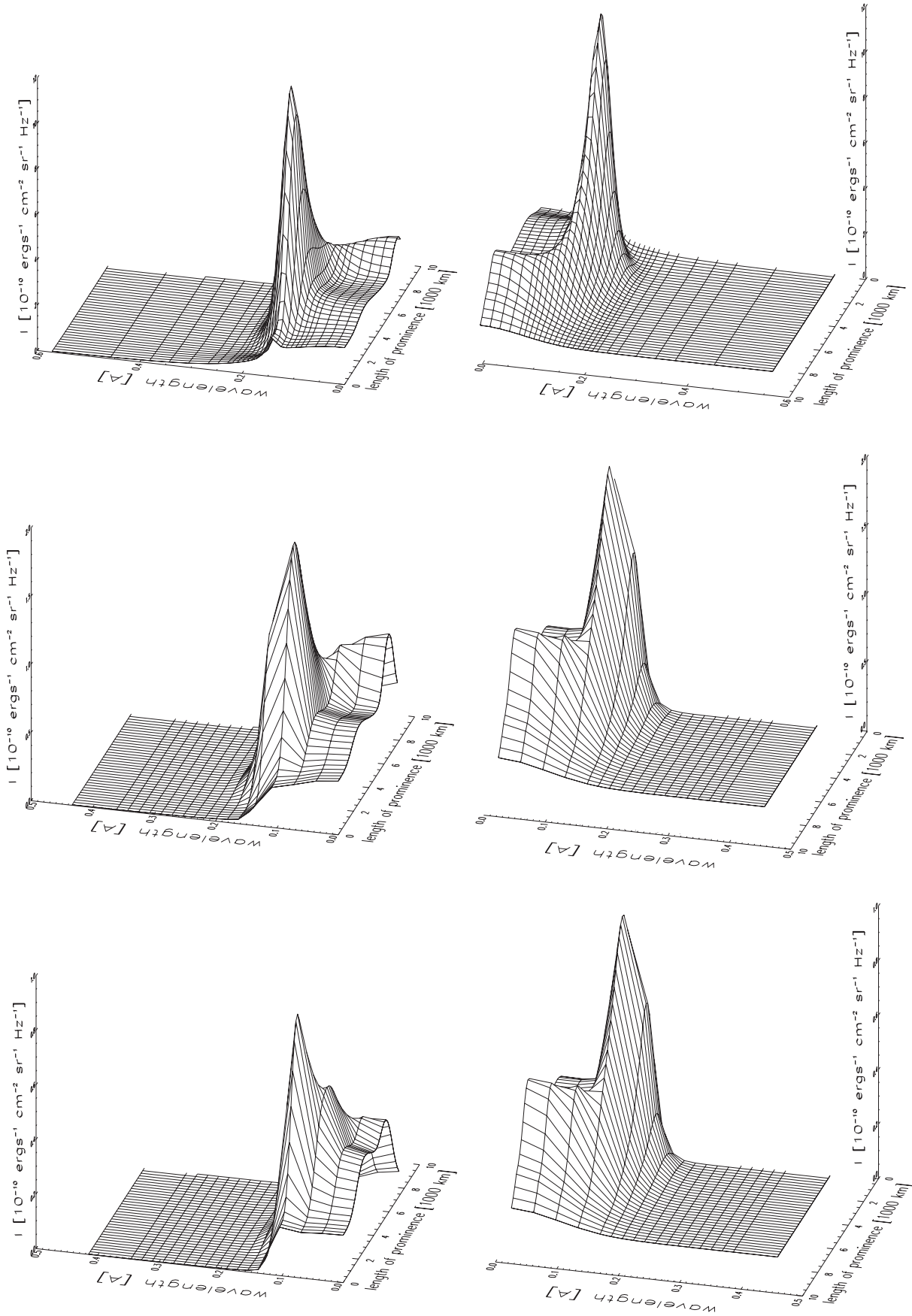


Fig. 4. The intensity plots for the lines of L β (pair of plots at the top), Ly (middle plots) and L6 (pair of plots at the bottom). On the left-hand side the structure is shown from the front, on the right-hand side from the rear.

in general the line profiles are much more reversed when we look along the y -axis (i.e. across the field lines). This trend becomes more pronounced when one goes to higher lines. The x -variation of the line intensity is shown for three different lines in Fig. 3. We can see that in the center of the structure (at $x = 0$) the reversal is not very pronounced, but it strongly increases outside the central parts. Finally, approaching the boundaries where $p \rightarrow p_0$, the profiles become unreversed with a central emission peak. This behaviour can be understood as follows. First, we have to realize that the temperature structure across the field lines is rather flat in the inner parts and only very near to the boundaries the temperature steeply increases to values of the surrounding corona – see Eq. (4) and the contours in the plots of the contribution functions). On the other hand, along the field lines (along the x -direction), the central temperature increases much more gradually (Eq. (3)). Let us now assume that looking across the field lines, we see different “slabs” of thickness of 1000 km, having temperatures gradually increasing from $T_0 = 8000$ K to T_{tr} . At the same time, the gas pressure decreases. It was demonstrated already by Gouttebroze et al. (1993) that in the case of isothermal-isobaric finite prominence slabs, the Lyman-line reversals strongly increase when the temperature starts to exceed $8\text{--}10 \times 10^3$ K and if also the pressure is sufficiently high. This is exactly what we observe outside the innermost parts of our 2D configurations. This behaviour can be understood by looking at the line source-function variations along the line-of-sight. The slabs are strongly irradiated from the solar surface and if the corresponding radiation temperature is comparable to the slab temperature, the line source function is only weakly decreasing towards the irradiated slab surface. However, by increasing the slab temperature, the source function starts to increase in the slab interior and decreases towards to surface. This naturally produces a strong reversal in Lyman lines, unless the gas pressure is so low that the whole line goes into emission (i.e. when it becomes optically thin).

5.2. Dependence on the shape of temperature structure

The shape of the temperature structure is fully described by the exponents γ_1 and γ_2 . For the discussion of effects of the temperature structure on the line profiles it is useful to compare two models which differ only in one of these parameters.

5.2.1. Effect of the exponent γ_1

Here we compare models A_1 and C_1 which differ in γ_1 ($\gamma_1 = 5$ for A_1 and $\gamma_1 = 10$ for C_1). We demonstrate the effect of changes of the exponent γ_1 on various lines.

$L\alpha$ and $L\beta$

The center of these spectral lines for both directions of view forms at the boundary of the prominence structure (Fig. 8), in areas with a high temperature rising up to the boundary value of 50 000 K where p goes to coronal pressure p_0 . The value of the $L\alpha$ central intensity is almost the same for both directions of view and for both models. Model A_1 gives the higher value

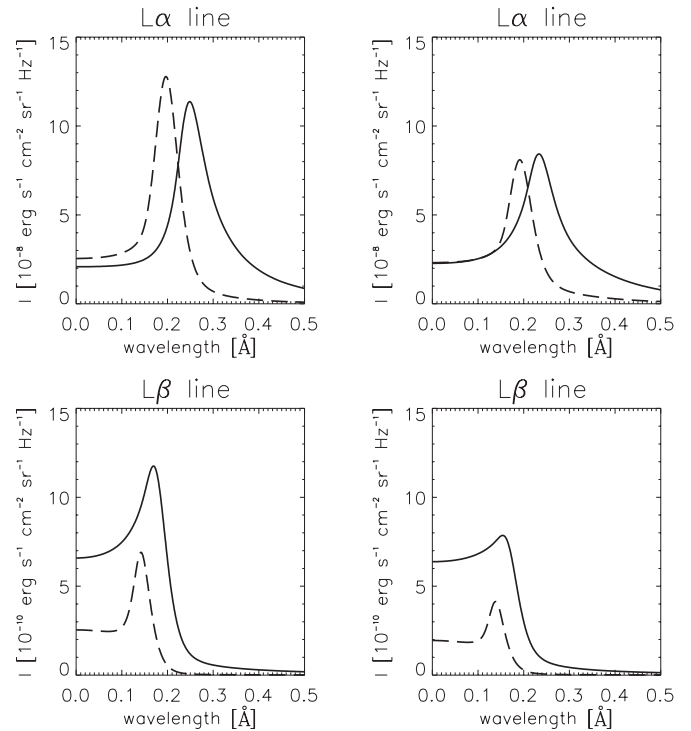


Fig. 5. Profiles of $L\alpha$ and $L\beta$ for model A_1 (left-hand side) and C_1 (right-hand side). Full lines are y -mean profiles, dashed lines are x -mean profiles.

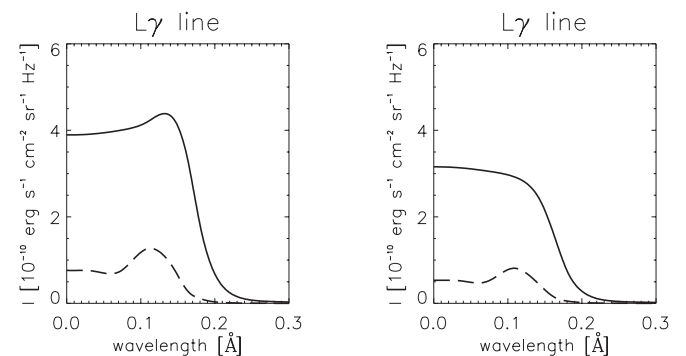


Fig. 6. Profiles of $L\gamma$ for model A_1 (left-hand side) and C_1 (right-hand side). Full lines are y -mean profiles, dashed lines are x -mean profiles.

of a specific intensity in the line peak (more than 40%) compared to model C_1 (Fig. 5). This is due to a higher temperature in the region of the peak formation (Fig. 8). The temperature is higher because we keep the boundary temperature fixed and have a lower temperature gradient close to the boundary for A_1 , given by the lower value of the parameter γ_1 . The wings of spectral lines are mostly optically thin and originate in the center of the thread (Fig. 8), the place with a low temperature, high density and negligible influence of the parameter γ_1 .

$L\gamma$

The region of formation of the line center is now deeper inside the structure. This leads to a higher value of the specific intensity in the center of $L\gamma$ for A_1 (up to 20%) in comparison to C_1 (Fig. 6) which is due to higher temperature in the region of origin of the line center (similarly as for $L\beta$). The mean

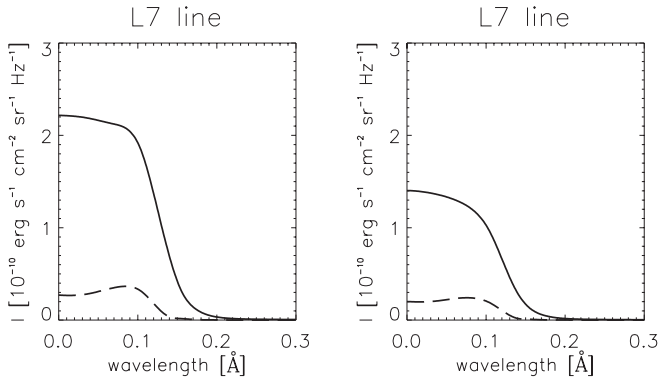


Fig. 7. Profiles of L7 for model A_1 (left-hand side) and C_1 (right-hand side). Full lines are y -mean profiles, dashed lines are x -mean profiles.

profile over y for the model A_1 has a weak self-reversal, while for C_1 the y -averaged profile is in emission (Fig. 6). This is again due to temperature differences. The mean profiles over x for both models still have a self-reversed shape (see discussion in Sect. 5.1), however the value of the specific intensity for A_1 is higher by some 20% than for model C_1 . The line wings are formed in the prominence center with negligible influence of the parameter γ_1 .

L δ –L11

The mean-profiles over y are in emission while the mean profiles over x show self-reversal for both models (Fig. 7). This is again consistent with our interpretation given in Sect. 5.1. The central and peak-intensities of the model A_1 are higher by some 40%. The line wings of lines L δ –L7 originate in the central part with the lowest temperature. The place of origin of the spectral lines L8–L11 is however shifted into regions with higher temperature which is required for the formation of these high-frequency lines (Fig. 9).

5.2.2. Effect of the exponent γ_2

Now we compare models B_1 ($\gamma_2 = 60$) and C_1 ($\gamma_2 = 30$).

L α

The line center originates from the boundary for both models and the values of the central intensity are identical. The place of formation of the peak intensity is shifted into the structure and the value of the specific intensity for model C_1 is higher (up to 30%) compared to the model B_1 (Fig. 11). It is due to the shape of the temperature structure (Fig. 12). The profiles for both models and for each direction of view have a self-reversal. The line wings, formed in the center of the thread, are not affected by the parameter γ_2 .

L β

The central intensity is again influenced by the shape of the temperature structure and for C_1 is higher by about 20%. The C_1 profile has a deeper self reversal while for B_1 the self reversal is quite negligible (Fig. 13). This is due to the formation of the peak in model C_1 in places with higher

temperature than in model B_1 (Fig. 14). The line wings again form in the central regions.

L γ –L11

The mean profiles over y are in emission for both models. For model C_1 , the x -averaged profiles show a self-reversal, but B_1 profiles averaged over x are in emission.

5.2.3. Line-center intensity for the Lyman series

In order to demonstrate how the Lyman series can be used to diagnose the thread structure, we plot in Fig. 10 the contribution functions at the line center of L α to L10, as viewed along the magnetic-field lines. This clearly shows that higher members of the Lyman series do form deeper and thus their line-center intensity reflects the temperature and density variations through the structure.

Figure 10 shows that the L α line center is formed at rather high temperatures, around 50 000 K or even more. We have made some test simulations with $T_{tr} = 10^5$ K and for such models the L α line-center formation region is entirely between 50 000 and 10^5 K. However, the actual mechanism of the line formation at these regions largely depends on the density. At the boundary where the gas pressure reaches values $p_0 = 0.03$ dyn cm $^{-2}$ in our models, the particle number density is almost two orders of magnitude lower than at the central cool regions. Therefore, the scattering of incident radiation can still play a role in determining the line source function, together with collisional excitations. According to our plots of L α profiles, the central intensity is roughly a factor of two larger than that of the diluted quiet-Sun intensity.

5.3. Effect of the field intensity variation

The value of the magnetic-field intensity has an essential effect on the shape of the prominence structure. We show the effect of field intensity variation for models A_3 ($B_x(0) = 2$ Gauss) and A_{3_1} ($B_x(0) = 10$ Gauss). Due to the lower value of the field intensity the model A_3 has a length around 5000 km while model A_{3_1} is 10 000 km long. Changes of the x -dimension cause different distributions of density inside the prominence structure.

L α

The line profile for model A_3 has a sharp self-reversal shape for both directions of view, different from model A_{3_1} (Fig. 15). A higher value of the peak intensity (up to 30%) for model A_3 is due to the higher temperature in the place of origin of the peak (Fig. 16).

Other spectral lines

The other line profiles are not reversed, for both models and directions of view (when averaged over x -direction). A_3 profiles have higher values of the specific intensity due to higher temperatures.

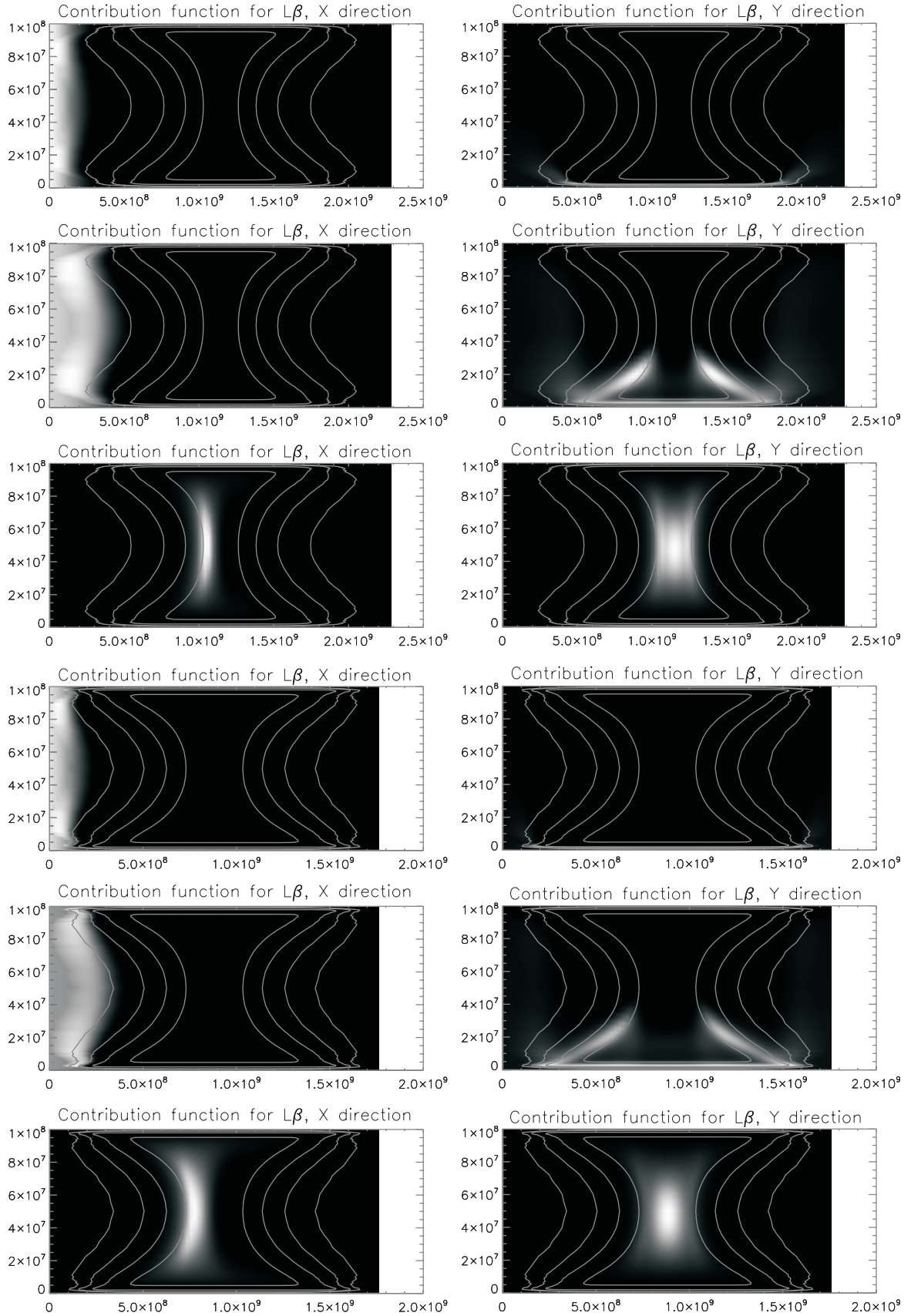


Fig. 8. $L\beta$ contributions as functions of x and y . The first six panels are for model A_1 , the other six for model C_1 . On the left-hand side the viewing is in the direction along the x -axis (from the left side), on the right-hand side in the y -direction (from the bottom). The upper pairs of each model are for the central frequency, the middle pairs are for the peak frequency and the lower ones represent contributions in the line wings. $x - y$ dimensions are in cm.

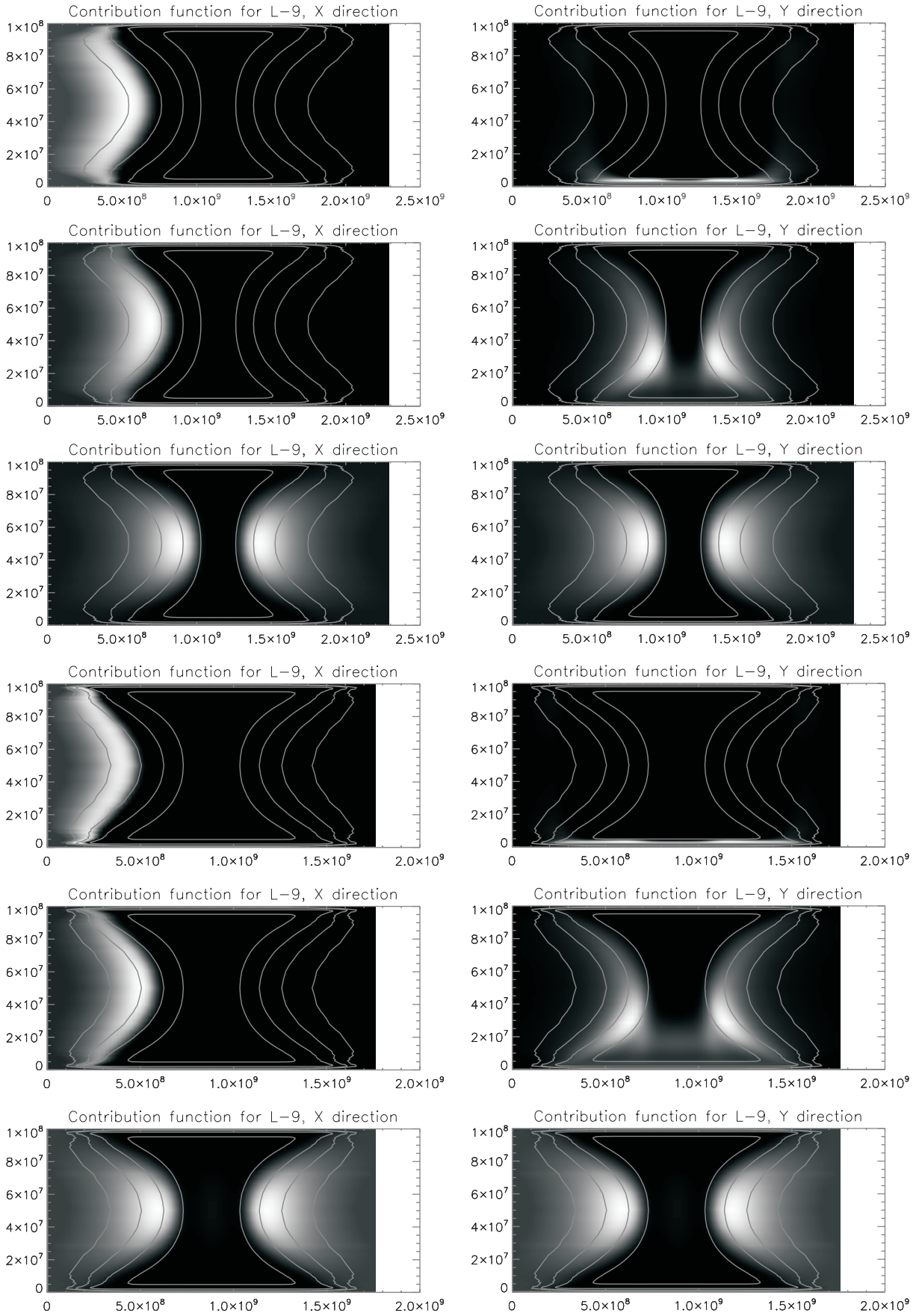


Fig. 9. L9 contributions as functions of x and y . The first six panels are for model A_1 , the other six for model C_1 . The figure is arranged in the same way as Fig. 8.

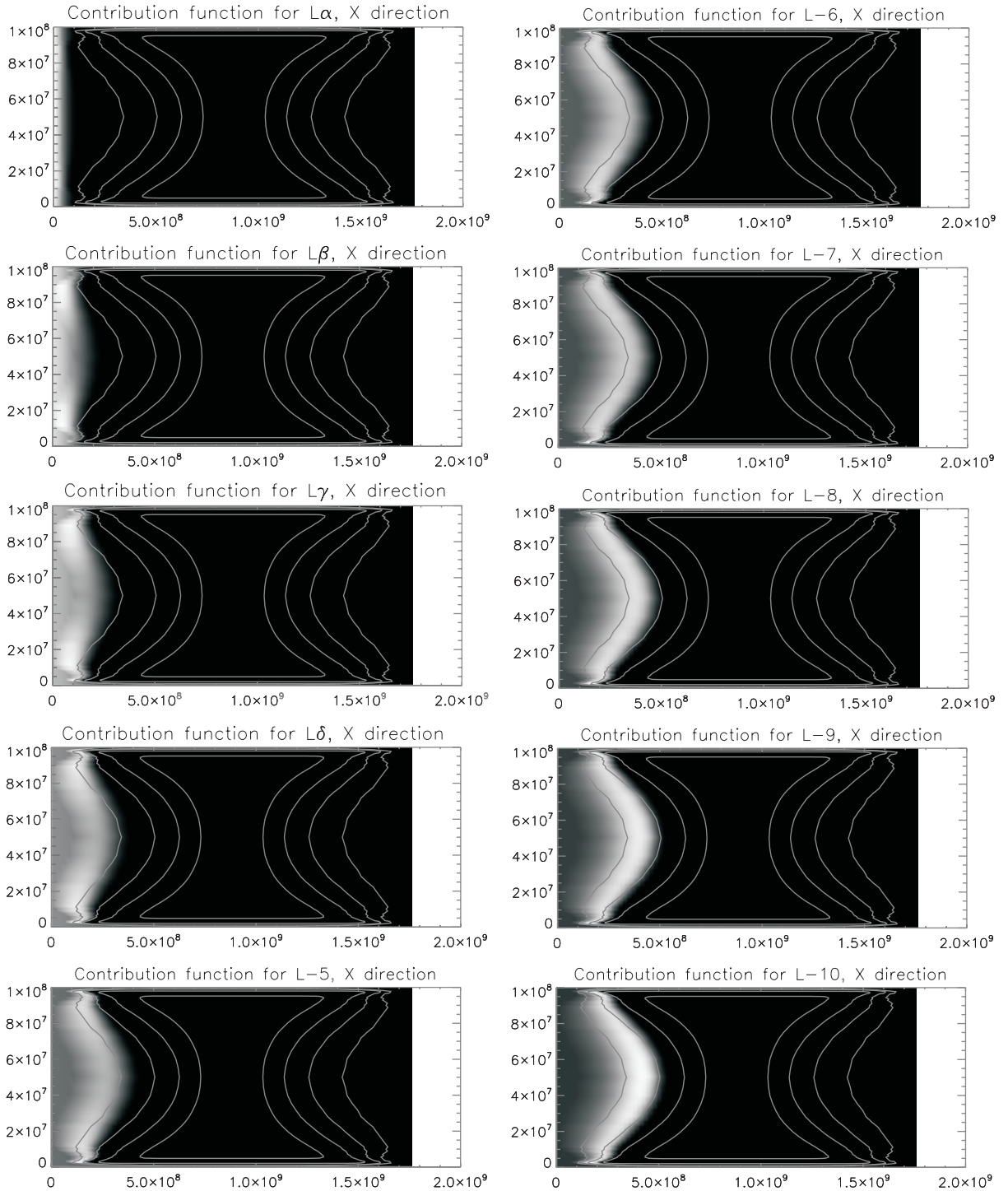


Fig. 10. Depth-variations of the line-center contribution function for the Lyman series ($L\alpha$ to $L10$), as viewed along the field lines. The model A_1 was used.

6. Geometrical shape of the thread structure

The geometrical shape of the prominence fine structure, i.e. its horizontal cross-section, is determined mainly by the magnetic field strength and the column mass, and to some extent also by the temperature structure. Variations of the input parameters for our 18 models have an essential effect on the magnetic field structure (dip) and therefore lead to different extensions in x -direction. In Fig. 17 the geometrical shape of all models is

shown. Each of these models has a fixed width of 1000 km in y -direction. The extension in x -direction (along magnetic field lines) is for each model represented by the length of the black bars.

Now we shall briefly analyse the effect of each input parameter on the geometrical length of the threads. The higher values of $B_x(0)$ give more extended thread structure due to larger magnetic tension force (dips can be less deep). This is clear from

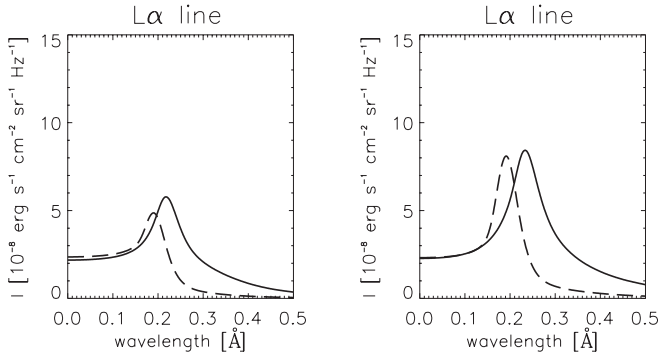


Fig. 11. Profiles of $L\alpha$ for model B_1 (left-hand side) and C_1 (right-hand side). Full lines are y -mean profiles, dashed lines are x -mean profiles.

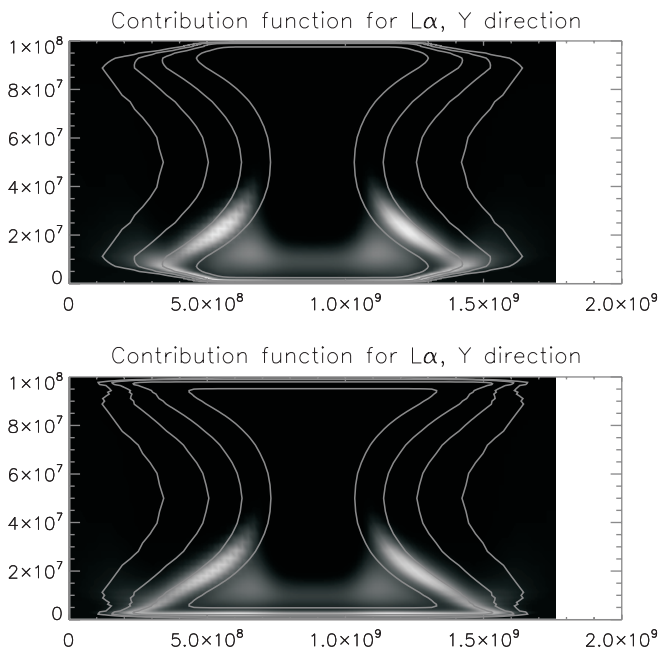


Fig. 12. $L\alpha$ contribution functions for model B_1 (top) and C_1 (bottom), showing the contributions for the peak frequency for observation in y -direction.

a comparison of the models with labels **3** and **3_I** and those labelled **4** and **4_I**. Models with labels **1** and **3_I** have comparable values of $B_x(0)$ but different values of M_0 . The larger extension of models **1** is due to the larger amount of mass in the structure. The temperature structure described by the γ parameters has also an influence on the density distribution in the thread. The shallower the increase of temperature, the more extended is the structure of the thread.

The actual shape of the structure as it would be projected onto the solar disk is somewhat more complex, but it retains features from Fig. 17. Restricting the thread to a finite vertical extension, one can use the 2D horizontal distribution of the vertical opacity (optical thickness) to compute e.g. the $H\alpha$ line contrast against the solar disk. For this a simple cloud model with the constant source function can be applied (see e.g. Heinzel & Anzer 2005). The resulting dark fibrils are rather long, their aspect ratio depends on the fixed thickness in y -direction which we took here to be 1000 km. In reality,

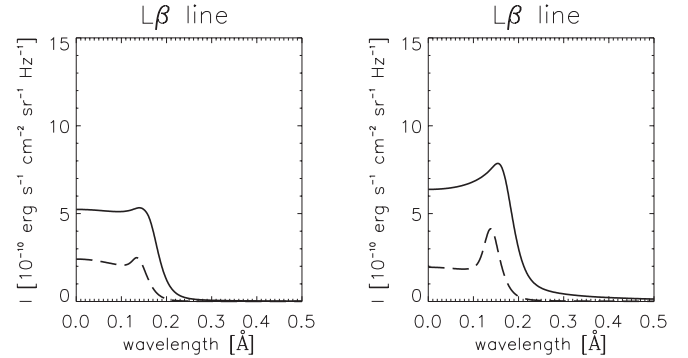


Fig. 13. Profiles of $L\beta$ for model B_1 (left-hand side) and C_1 (right-hand side). Full lines are y -mean profiles, dashed lines are x -mean profiles.

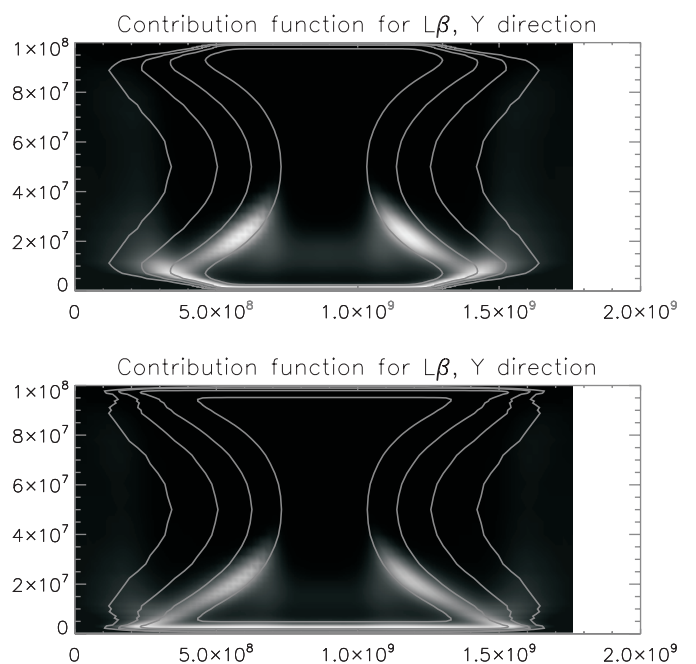


Fig. 14. $L\beta$ contribution functions for model B_1 (top) and C_1 (bottom), showing the contributions for the peak frequency for observation in y -direction.

however, this thickness can be smaller and thus the fibrils could appear long. This situation resembles recent high-resolution (up to about 0.2 arcsec) $H\alpha$ images obtained either with the new SVST or with DOT on La Palma (see Engvold 2005; or DOT website). We interpret the central parts of *quiescent* filaments as being composed of shorter, densely packed fibrils which are in fact the magnetic dips projected onto the disk – see also Aulanier & Démoulin (1998, 2003). Very long individual fibrils which extend out of the filament body may have different nature, they can correspond to low-lying extended fluxtubes with significant horizontal flows (Engvold 2005).

7. Discussion and conclusions

Let us now comment briefly on the models of Fontenla et al. (1996). These models were aimed, as ours here, to represent the vertical fine-structure threads of quiescent prominences. But in

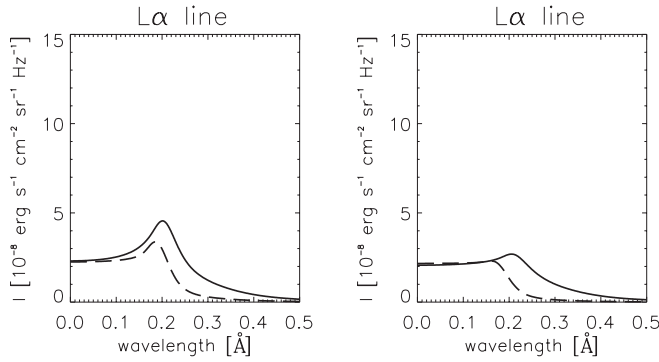


Fig. 15. Profiles of $L\alpha$ for models A_3 (left-hand side) and A_{3_1} (right-hand side). Full lines are y -mean profiles, dashed lines are x -mean profiles.

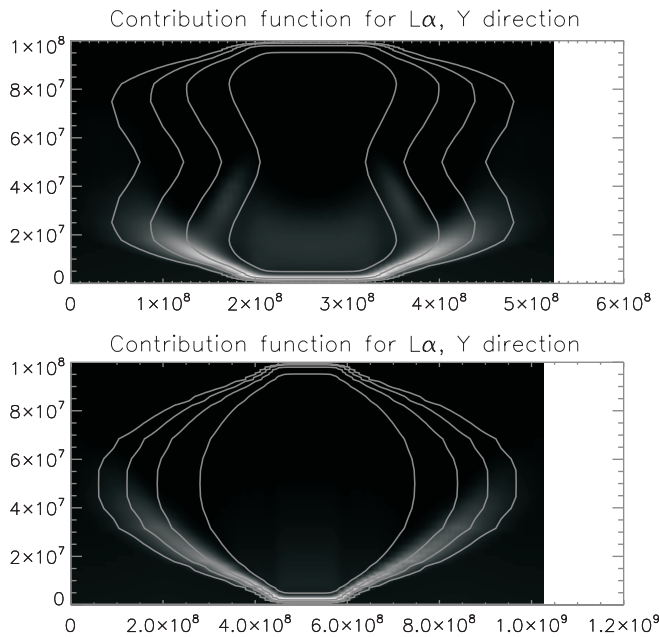


Fig. 16. $L\alpha$ contribution functions for model A_3 (top) and A_{3_1} (bottom), showing the contributions for the peak frequency for observation in y -direction.

contrast to our models they consider 1D isobaric slab configurations. Their approach is in some respect complementary to ours: they determine the temperature structure in the slab from the condition of energy balance (assuming some kind of heating function and taking the energy transport by ambipolar diffusion into account). But they do not solve the MHS equilibrium equations. In contrast to this we solve the 2D MHS equilibrium, but prescribe ad hoc temperature profiles ignoring the energetics. Also the geometries of the two sets of models are very different: Fontenla et al. (1996) take a very large number of extremely thin slabs (just a few tens km each) which are perpendicular to the magnetic field (see also discussion by Anzer & Heinzel 1999), while we study individual 2D threads aligned with the magnetic field. Fontenla et al. (1996) considered several 1D slabs (threads) along the line-of-sight and the emergent synthetic intensities were computed for Lyman lines (also using PRD for $L\alpha$ and $L\beta$). Comparing this to our 2D models, two problems arise. First, in our MHS scenario, only one

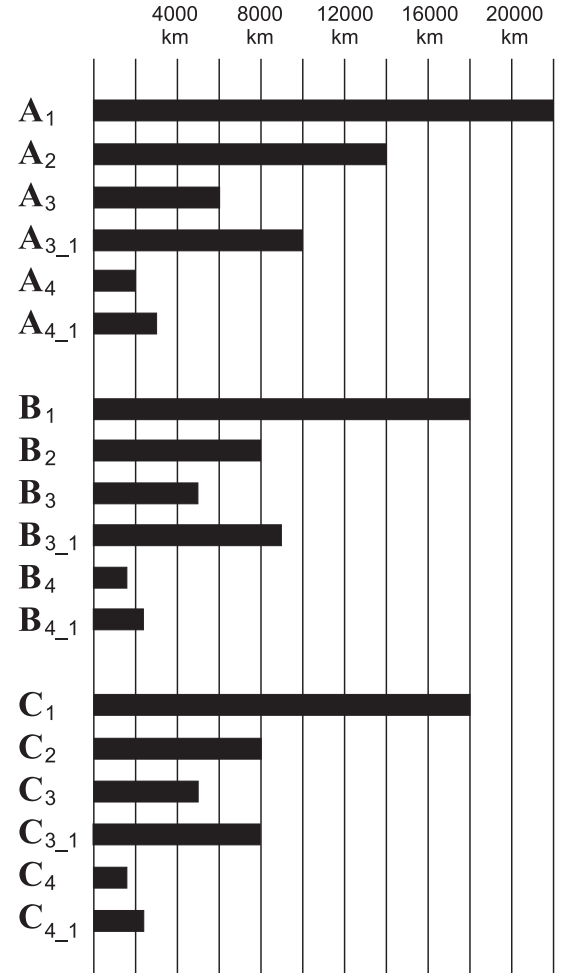


Fig. 17. The geometrical shape of all models. Each bar has a width of 1000 km.

thread (dip) is allowed along the given field line, others being formed along nearby lines. This then means that looking strictly along the field lines, we can see only one thread, not a multithread structure. However, our 2D approach allows us to look also across the field lines and then we can see several threads along the line-of-sight. Considering the energy balance in the way similar to Fontenla et al. (1996), in 2D one could compute the ambipolar diffusion along the field lines, but look through several threads perpendicularly. The second problem is that the models of Fontenla et al. (1996) are very narrow along the magnetic field, while ours show a rather long extension in this direction (see Fig. 17). This is a direct consequence of the MHS equilibrium and the empirical temperature structure.

Another comment concerns the assumption that the threads are very extended vertically, in fact we take them as vertically infinite in our 2D approach. The idea comes from Poland & Mariska (1988) who suggested that when a dip is formed locally the field below becomes compressed and that above diluted. Therefore the dip region grows in height, by vertical propagation and thus forms a thread filled by cool plasma. However, the real vertical extension is difficult to estimate. From the observational point-of-view, one should try to derive the vertical extension from high-resolution disk observations of

filaments (see discussion in Sect. 6), from the theoretical side a 3D MHS configuration should be constructed and then used for fully 3D transfer modelling.

We discuss how the magnetic field configuration of a vertical prominence thread can influence the structure of the prominence–corona transition region. As we show, depending on this structure one obtains different line profiles for the series of Lyman lines, namely when looking, respectively, *along* and *across* the magnetic-field lines. Studying these lines can give us important information on the physical conditions in the prominence threads. In the next paper we intend to apply this modelling to sets of Lyman-line profiles observed in prominences by SOHO/SUMER. By searching for the best fit simultaneously to all observed Lyman profiles one should be able to determine in detail the physical structure of prominence threads. However, this may require a more complex modelling based on multi-thread configurations – several threads seen along the line-of-sight which passes across the magnetic-field lines.

Acknowledgements. P.H. acknowledges the support from MPA Garching, U.A. thanks for support of the Ondřejov Observatory. This work was done in the frame of grant No. IAA 3003203 of the Grant Agency of the Academy of Sciences of the Czech Republic, ESA-PECS project No. 98030 and the research project AVOZ10030501. SOHO is a space mission of international cooperation between ESA and NASA. The authors thank to P. Gouttebroze and J.-C. Vial for their valuable comments.

References

- Anzer, U., & Heinzel, P. 1999, A&A, 349, 974
 Auer, L. H., & Paletou, F. 1994, A&A, 285, 675
 Aulanier, G., & Démoulin, P. 1998, A&A, 329, 1125
 Aulanier, G., & Démoulin, P. 2003, A&A, 402, 769
 Engvold, O. 2005, in *Multiwavelength Investigations of Solar Activity*, ed. A. V. Stepanov, E. F. Benevolenskaya, & A. G. Kosovichev (Cambridge Univ. Press), Proc. IAU Symp., 223, 187
 Fontenla, J. M., Rovira, M., Vial, J.-C., & Gouttebroze, P. 1996, ApJ, 466, 496
 Gouttebroze, P., Heinzel, P., & Vial, J.-C. 1993, A&AS, 99, 513
 Heasley, J. N., & Mihalas, D. 1976, ApJ, 205, 273
 Heinzel, P., & Anzer, U. 2001, A&A, 375, 1082 (Paper I)
 Heinzel, P., & Anzer, U. 2003, in *Stellar Atmosphere Modeling*, ed. I. Hubeny, D. Mihalas, & K. Werner, ASP Conf. Ser., 288, 441
 Heinzel, P., & Anzer, U. 2005, in *Solar Magnetic Phenomena*, ed. A. Hanslmeier, A. Veronig, & M. Messerotti, Astron. Astrophys. Space Sci. Lib., 320 (Dordrecht: Springer), 115
 Heinzel, P., Gouttebroze, P., & Vial, J.-C. 1987, A&A, 183, 351
 Heinzel, P., Schmieder, B., & Vial, J.-C. 1997, in *Proc. Fifth SOHO Workshop*, ESA SP-404, 427
 Heinzel, P., Schmieder, B., Vial, J. C., & Kotrč, P. 2001, A&A, 370, 281
 Mihalas, D., Auer, L. H., & Mihalas, B. 1978, ApJ, 220, 1001
 Paletou, F. 1995, A&A, 302, 587
 Paletou, F., Vial, J.-C., & Auer, L. H. 1993, A&A, 274, 571
 Patsourakos, S., & Vial, J.-C. 2002, Sol. Phys., 208, 253
 Poland, A. I., & Mariska, J. T. 1988, in *Dynamics and Structure of Solar Prominences*, Proc. of a Workshop held at Palma de Mallorca, ed. J. L. Ballester, & E. R. Priest, Universitat de les Illes Balears, 133
 Schmieder, B., Heinzel, P., Kucera, T., & Vial, J.-C. 1998, Sol. Phys., 181, 309
 Schmieder, B., Heinzel, P., Vial, J.-C., & Rudawy, P. 1999, Sol. Phys., 189, 109
 Schmieder, B., Tziotziou, K., & Heinzel, P. 2003, A&A, 401, 361
 Vial, J.-C. 1982, ApJ, 254, 780
 Warren, H. P., Mariska, J. T., & Wilhelm, K. 1998, ApJ, 119, 105